International Journal of Impact Engineering 184 (2024) 104828

Contents lists available at ScienceDirect

International Journal of Impact Engineering

journal homepage: www.elsevier.com/locate/ijimpeng

# A new compact, self-compressing, vertical one and two-stage gas gun at the University of Kent

M.C. Price [a,b], M.J. Cole [a], K.H. Harriss [a], L.S. Alesbrook [a], M.J. Burchell [a,#], P. J. Wozniakiewicz [a,*]

[a] Center for Astrophysics and Planetary Science, School of Physics and Astronomy, University of Kent, Canterbury, Kent CT2 7NH, UK
[b] Odin Space Ltd, London WC1 8HN, UK

ARTICLE INFO

*Keywords:*
Vertical gun
Two-stage light gas gun
Granular targets
High speed impacts

ABSTRACT

A new gas gun configuration has been developed at the Centre for Astrophysics and Planetary Science, University of Kent, to produce vertical impacts at up to 2 km $s^{-1}$. The vertical arrangement allows impact into non-cohesive target materials such as sand (representing loose regolith on the surface of solar system bodies) and water. Three key constraints had to be met: (1) the vertical gun had to fit in a laboratory with a ceiling of 3.5 m height, (2) the gun had to operate without a chemical propellant (i.e. gunpowder) and (3) it had to fire into the same target chamber as the existing horizontal Kent gun. In addition, the use of standard pipeline elements was adopted. The result was a self-compressing right angle shaped gun design, with single and two-stage variants for low and high speeds respectively. The gun assembly and its operation are described, together with ancillary components. The self-compressing first stage of the gun (using pressure generated by boiling liquid nitrogen) is horizontal leading into a vertical second stage. The gun has performed as expected, with shots in the speed range 0.3 to 2 km $s^{-1}$. Results from the first study using the gun are presented for impacts of 1 mm diameter stainless steel spheres into sand over the full speed range, and are found to be compatible with previous work at low and high speed.

## 1. Background

The University of Kent (UK) has had a horizontal two stage light gas gun since 1989 [1,2], simulating impacts relating to solar system research (ranging from planetary science to aerospace engineering) as well as studying the underlying shock physics. Two-stage guns were first described by [3], and the Kent gun is typical of its kind. A general description of the various such guns in current or recent use is available in [4] who list over 60 such guns operational worldwide since the 1990s. Almost all of these guns fire horizontally, with just a few capable of firing vertically, e.g., NASA-Ames, US [5], the Open Univ., UK [6], NASA-Johnson Space Centre, US [7] and ISAS/JAXA, Japan [8].

Two-stage guns compress a light gas in the first stage, typically via an external compressor or, as in the original horizontal Kent gun, by use of a piston driven by detonation of a chemical propellant (gunpowder loaded in the laboratory into a shotgun cartridge). This highly compressed gas is then released when a bursting disk separating the two stages ruptures at high pressure, quickly releasing the light gas into the second tube, called the launch tube. A plastic or nylon sabot is placed immediately behind the bursting disk (at the entrance to the launch tube) and is accelerated by the expanding light gas down the length of the launch tube into the range of the gun. The Kent horizontal gun fires plastic sabots approximately 4.4 mm in diameter, at speeds typically ranging from 1 to 7.5 km $s^{-1}$, with the maximum speed ever achieved being some 8.4 km $s^{-1}$. The shot speed can be selected pre-shot by varying the type and amount of gunpowder used and the nature, and degree, of pre-shot pressurization of the light gas. It is also possible to vary the speed slightly by changing the mass of the piston used to pressurize the light gas in the first stage, and by adjusting the pressure at which the busting disk ruptures (by changing the material used for the disk or scoring it).

If single-piece, solid projectiles (these are the same dimensions as split sabots, but are solid cylinders of nylon 6,6) are used, they can be fired from a smooth bore launch tube, or, a rifled barrel can be used to spin the sabot to aid stability in flight. If a split sabot is used (typically 2 or 4 interlocking pieces), rifled barrels are always used, causing the sabot to spin. The sabot pieces then fly apart and separate after exiting

* Corresponding author.
*E-mail address:* P.J.Wozniakiewicz@kent.ac.uk (P.J. Wozniakiewicz).
# Submitting author

https://doi.org/10.1016/j.ijimpeng.2023.104828
Received 28 July 2023; Received in revised form 20 October 2023; Accepted 14 November 2023
Available online 21 November 2023

the launch tube. Such split sabots are used to launch smaller projectiles, which are placed in a hollow central shaft in the sabot. A stop plate collects the (off-axis) sabot pieces, whilst the load (on the main axis) passes through a central hole in the plate and proceeds to the target. In this way, single projectiles from approximately 0.5 mm up to 3.5 mm can be fired in the gun. These can be of a variety of compositions and shapes. Smaller projectiles can also be fired when placed into the split sabot as a buckshot load, with multiple smaller projectiles reaching the target in a single shot, usually at a similar speed to within a range of around 4 – 5 %.

The original lower speed limit in the gun (around 1 km $s^{-1}$), was overcome by effectively turning the gun into a single stage gas gun. This was achieved by injecting pre-pressurized gas into the pump tube, and then, without any further compression from a piston, breaking a bursting disk made of a weaker plastic or a modified bursting disk by melting it with an electric current (see [2]). The released gas then drives the sabot into the range of the gun. Speeds as low as 300 m $s^{-1}$ can be achieved with this set-up, permitting the same projectiles to be launched at targets over a wide speed range so the transition from low-, to high-speed impacts can be more fully observed in a single facility, with the same gun.

Data from the horizontal Kent gun has appeared in over 100 refereed papers, covering topics such as aerospace engineering (e.g. [9,10]), planetary science (e.g., [11,12]), shock physics [13,14], organic materials under impact [15,16], and impacts on biological and related materials [17,18]. There has always been a limitation, however, with horizontal guns in that they need targets to be mounted vertically for normal incidence impacts, and this is not easy for targets with little, or no, internal cohesion and which would naturally prefer to have a horizontal and not vertical surface. It is possible to tilt the entire gun and fire at non-normal incidence (either at a fixed vertical angle, or a variable angle) into a horizontal target's surface. This brings its own complexities, including for example, a vertical or adjustable mounting is required, flexible connections for vacuum lines etc. are needed, and an arrangement has to be made to the target chamber either to permit access at any angle or at fixed angles. This has been done elsewhere, at, for example, NASA Ames [5] and the Open University (UK) [6]. However, ignoring the other issues, simply tilting the entire Kent gun range to achieve vertical impacts, would require a laboratory with an internal height of over five metres; this is unavailable at Kent, and would thus require a new building. For granular materials, a horizontal gun could be used and the target surface inclined at up to approximately 20° from horizontal for impact. The exact limit depends on the coefficient of friction of the material, remembering that the most extreme vertical slope of any resulting crater needs to be below the angle for collapse of the material. Given that the typical impact angle for an object hitting an atmosphereless planetary surface is 45°, this results in limited applications of such impacts. Shallow angle impacts into sand targets have, however, been carried out in the horizontal gun at Kent to simulate the end of life collision of the Smart-1 spacecraft into the lunar surface [18–20]. Impacts into liquids have been achieved by placing the liquid in a bag, or behind a thin membrane. This has been done at Kent, to study, for example, crater shape in rocky floors of oceans with overlying water layers at the moment of impact [21] or in water-saturated porous targets [22]. However, such experiments are limited in their nature, and the ability to use a vertical gun would be beneficial.

The requirement for a compact vertical gun contained within the existing, limited, laboratory space, has thus led to development at Kent of a right angle shaped gun which effectively fires around corners, at speeds up to 2 km $s^{-1}$.

## 2. Gun design

The new, "vertical" gun utilizes two key ideas. The first is based on the realization that a two-stage gun does not have to have the two stages arranged in a straight line. Essentially, the connection between the two stages can be at any angle, as long as the gas is released efficiently from the pump tube into the launch tube. The result is a right angle shaped gun, where a horizontal first stage is coupled via a right-angled bent connection, into a vertical second stage, as shown in Fig. 1.

The second idea was to use a self-compressing gas in the first stage. The method used is a gas reservoir connected to the pump tube by a fast-acting valve to insert the gas into the first stage. To keep the cost low, and regulatory compliance procedures simple, standard commercially available pipework was selected for the reservoir. The gas reservoir and attendant gas handling are shown in Fig. 2. The method chosen for pressurizing the gas reservoir was to allow a small volume of liquid nitrogen to boil into nitrogen gas, so pressurizing the reservoir with nitrogen gas. Here the maximum pressure obtained was 340 bar. Higher pressure is possible with this method but is limited by the maximum pressure capability of the reservoir tubing and the pressure rating uncertainty of the pressure safety burst disc. Using this method, the reservoir is pressurized with relatively pure and dry nitrogen gas.

Not using gunpowder-based shotgun cartridges at an awkward height in the laboratory (i.e. close to the ceiling), or an external compressor pump (e.g. as at the University of New Brunswick, Canada, impact facility, [23]) offers several attractive features. Dispensing with the gunpowder solves four problems - handling gun cartridges at height, the variable availability of the rifle-powder, removing the excessive energy of gun cartridges, and removes gunpowder residues from the system resulting in a cleaner gun. Not using an external compressor minimizes high-pressure lines and associated equipment in the laboratory. Such a compressor could, for example, use a nitrogen or helium gas feed, a ballast tank on its outlet and water and oil separation to keep the gas pure. The choice was made, however, to try the liquid nitrogen method to see if it would be practicable. The lower complexity of the system, the ready availability of liquid nitrogen and the smaller equipment volume are in its favor, but arguably, more operator intervention is required, although more automation could, potentially, be added to mitigate this.

### 2.1. Mechanical design

As the vertical gun was developed from an existing horizontal gun, the original design (a 1 m long, ½" bore pump tube and 0.7 m long,


**Fig. 1.** Photograph of the new gun assembly. The horizontal first (pump) stage (H) is at the top of the image and the vertical second stage (V) (launch tube) assembly at the left. The central breech (C) is on the left-hand end of the horizontal pump tube. The right angle elbow then follows (E) connecting to the vertical launch tube. The larger internal diameter drift tube (D) physically connects the launch tube and the target chamber (T). The direction of the projectile as it enters the target chamber is indicated (P). The whole gun assembly is supported on two vertical steel columns (S), topped with a horizontal "I" beam fixed permanently in position (FI). The pump-tube and breech are mounted on a horizontal, rolling "I" beam (RI), which is in turn mounted on FI.

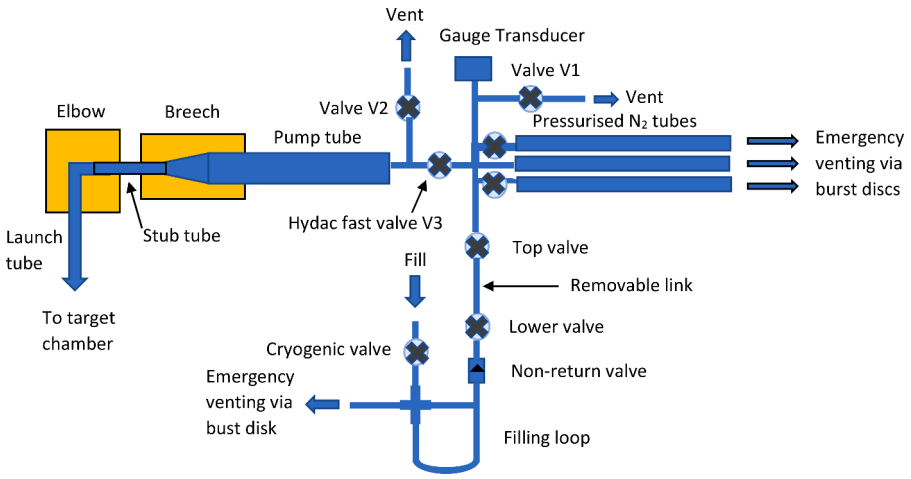


**Fig. 2.** Gas handling diagram system.

0.170″ bore launch tube), plus the central breech, were used without modification. A new gas reservoir was designed to connect to the upstream end of the pump tube, replacing the original shotgun cartridge holder. The reservoir consists of three stainless steel tubes (made of 316 alloy) arranged in parallel (see Fig. 2). These tubes are 1 m long and are 12 mm outer diameter with 2 mm walls. The two flank tubes can be isolated from the central one with valves, this allows some variability of the reservoir volume. Ideally, a single large diameter tube would be used for the reservoir with a bore greater than the pump tube diameter. However, this three-tube arrangement allows for use of lower cost 470 bar rated tubing, thus permitting 400 bar operation with a total internal cross-section 1.19 times the pump tube. Safety burst discs are fitted to the external end of each of the tubes, at a nominal pressure of 388 bar on the flanking tubes, and 373 bar on the central tube (these values are lower than the nominal design 400 bar to allow a safety margin). The connection of the combined reservoir to the pump tube is by 16 mm outer diameter fittings, which have a 12 mm, bore.

A fast-acting Hydac™ ball valve, rated at 400 bar with a measured opening time of 140 ms, separates the gas reservoir from the pump tube. A nylon-6,6 piston is placed at the up-range end of the pump tube. To guard against any gas leaks through the valve displacing the piston pre-shot, a small dead volume is maintained at the back of the piston until the shot. This can be vented to air if necessary. The gas reservoir, fast acting ball valve and small dead volume were bought as standard pipework components, but an adaptor between these and the pump tube was made from a 75 mm diameter cylinder of AISI 4150 steel.

The pump tube is connected to the central breech (which stops the piston), with an "O" ring seal between them. Unlike the existing gun, however, there is now a physical separation between the central breech and the launch tube. This is to allow the presence of the right-angled turn in the gun via the elbow joint. A stub tube 135 mm long, is used to connect the breech to the elbow. This stub tube connects to the horizontal opening in the connecting elbow, which is made from a block of AISI 4150 steel 150 mm long, 75 mm wide and 100 mm deep, shown diagrammatically in Fig. 3.

The gun launch tube is screwed into the vertical opening in the elbow connector. The launch tube presses against a scored aluminium burst disc, which forms a seal between the launch tube and the elbow. Pre-shot, the pump tube and elbow are filled with the gas that will eventually accelerate the projectile within its sabot. This pre-shot pressure depends on the final speed required: a typical shot uses hydrogen at around 10 bar. This gas is sealed at the upstream end by the piston and at

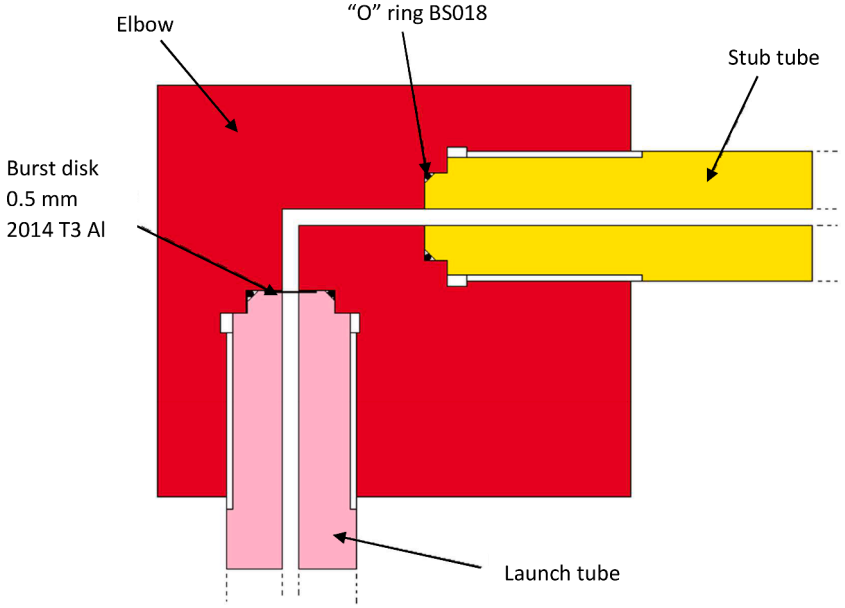


**Fig. 3.** Connecting elbow cross section.

the downstream end by the burst disk at the entrance to the launch tube. Immediately behind the burst disk, the launch tube contains a plastic sabot loaded with a projectile, which in this initial study was a 1 mm diameter stainless steel sphere.

When the gun is fired, the sudden release of the pressurised nitrogen (via action of the ball valve), drives the piston down the pump tube, similar to the firing of the shotgun cartridge in the original horizontal gun. The gas on the downstream side of the piston is thus compressed and eventually breaks the burst disk, releasing the compressed gas vertically into the launch tube, accelerating the sabot and projectile along the launch tube in a downwards direction. The projectile is held under compression in the sabot, so does not fall out pre-shot. Similarly, the sabot is a tight fit in the launch tube (to ensure a good gas seal around the sabot and prevent gas escaping around it), so does not slide down the launch tube pre-shot. The downstream end of the launch tube protrudes into a vertical drift tube (mounted on the top of the target chamber) using an 'O'-ring seal to maintain a vacuum in the target chamber. The drift tube allows the sabot segments sufficient flight distance to separate from the projectile before being intercepted by a stop plate mounted inside the target chamber. The target chamber is a cube-shaped vacuum chamber (usable internal dimensions 1.14 m by 1.14 m by 1.14 m and typically evacuated to less than 1 mbar pre-shot).

### 2.2. Filling the nitrogen reservoirs

Initially the gas reservoir system (Fig. 2) is charged with nitrogen gas, by closing vent valve V1 and using a sample cylinder, attached to a cryogenic Habonim™ ball valve, to transfer nitrogen from a larger cylinder kept outside of the laboratory. The large cylinder contains nitrogen gas at 200 bar (maximum) and the reservoir can typically be pressurized to between 120 and 160 bar via this method.

The nitrogen gas reservoir pressure is increased further by using a 'U' shaped filling loop (Fig. 2). It is made of the same tube type as the reservoir tubes; the height of the 'U' is 289 mm and was shaped in-house. With the cryogenic valve shut and the filling loop lower valve shut, the loop is immersed in liquid nitrogen to within a few centimeters from the top connections. Any existing nitrogen gas in the loop then condenses into liquid in the cooled loop, so the cryogenic valve can be opened without gas loss, and fresh liquid nitrogen can be poured in using a cooled funnel with a delivery tube that reaches to the top of the filling loop. With the funnel removed, the filling loop system is re-pressurized using nitrogen from the gas bottle as before and the cryogenic valve is then shut. *Re*-pressurizing this way avoids having to pressurize the dead volume above the loop using the boiling liquid nitrogen, so allows higher ultimate pressure in the reservoir. The liquid nitrogen bath surrounding the loop is then removed and the valves to the main gas reservoir opened. This allows the liquid nitrogen within the loop to boil into nitrogen gas, pressurizing the gas reservoir. Heating of the filling loop during this operation is achieved by a fan blowing room temperature air over the filling loop.

Five of the liquid nitrogen filling cycles, produces approximately 320 bar of nitrogen within the gas reservoir, at which point the reservoir can be isolated from the filling loop, plus its delivery tube, and the filling loop vented. The hydrogen pressure in the pump tube is then checked immediately before the shot.

Firing the gun consists of closing the dead volume vent valve V2 and then opening the fast action ball valve V3. This allows the nitrogen gas from the reservoir to push the piston horizontally in the pump tube, compressing the hydrogen gas ahead of the piston. At typically around 190 bar, the hydrogen pressure is high enough to rupture the aluminium burst disc and the hydrogen gas expands into the launch tube, accelerating the sabot and projectile vertically downward. Operation of the valves V1, V2 and V3 is done electronically by use of a firing box from a neighboring room, permitting safe firing of the gun.

The launch tube is rifled so upon exiting into the drift tube, the spinning sabot separates into its four component segments, typically 20 mm apart, which then enter the target chamber, along with the projectile, which continues on the central axis-of-flight. Within the target chamber a removable frame supports a blast tank which is a 200 mm cube shaped steel box (see top of Fig. 4), containing a steel stop-plate for the sabot segments. The blast tank has a 50 mm aperture in its top to allow the separated sabot segments entry and the stop plate has a 10 mm exit aperture to permit only the projectile to continue downward. Alignment of the gun to this 10 mm aperture is crucial to allow the projectile to hit the target. To achieve this, an LED light is attached to a replacement stop plate in the position of the exit aperture and is shone upward. A polished annular aluminium mirror with a black cross is permanently positioned on the end of the launch tube and the reflected light produces a cross on the replacement stop plate. This cross can be centered by moving the blast tank back and forth parallel to the pump tube axis and side-to-side by altering the relative tension on the two turnbuckles on the elbow anti-recoil stays. The replacement stop plate is removed pre-shot and the actual stop plate attached.

Connected to the base of the blast tank is a time-of-flight system, which has two laser LEDs 119 mm apart (Fig. 4). Each LED produces a red light beam approximately 15 mm wide and 1 mm deep, which is focused onto separate photo-diode detectors to give the projectile's time-of-flight over the 119 mm path. The data from the LEDs is read out onto digital storage oscilloscopes. The timing information gives a projectile speed accurate to ±0.5 % for mm sized projectiles (which give well-defined signals on the oscilloscope).

The target is placed below the time-of-flight system on the base of the target chamber, on top of a metal baseplate to protect the floor of the chamber from inadvertent projectile impact (Fig. 4).

### 2.3. Mounting frame

The pump tube portion of the gun is 3.1 m above floor level, and is held up by steel columns permanently attached to the floor (Fig. 1). Separately to this, the elbow connections to the launch tube and stub tube need to be protected from recoil forces. To save having a bracing structure attached to the building, the gun is therefore attached to the 1 tonne target chamber, as it is chiefly movement between these two elements that is to be avoided. Any recoil of the vertical launch tube is resisted by a removable strap, which passes over the elbow and is connected to the target chamber by two steel rope stays in an "A" configuration with each end of the rope tensioned by a turnbuckle. Horizontal recoil is generated when the piston is accelerated and stopped. The horizontal parts of the gun are mounted on a rolling, steel 152 × 152 mm "I" beam, allowing ease of access and movement during setup (Fig. 1). This beam is in turn clamped to a larger 254 × 146 mm supporting "I" beam, which is connected by a steel rope stay to the target chamber (Fig. 1). This is permanently connected as it does not interfere with gun usage, and no movement has been observed so far during operation.

The section of gun from pump tube to launch tube can be raised from the rolling beam and lowered again to insert the launch tube into the drift tube part of the target chamber. This section of gun is assembled at ground level and hoisted into position on a carriage that runs on tracks to save carrying the 32 kg assembly to the 3.1 m operating height.

## 3. Test shot program

The gun was tested in both single and two stage modes of operation, with repeated firings.

### 3.1. Single stage gun performance in test firings

The vertical gun was fired 11 times in single-stage mode to obtain low speeds, using 1 mm diameter stainless steel projectiles. A 0.25 mm thick acetate plain burst-disc with a 0.25 mm thick acetate annular backing was used to maintain the gas seal between the pump and launch tubes. The pump tube pressure was simply increased until the acetate

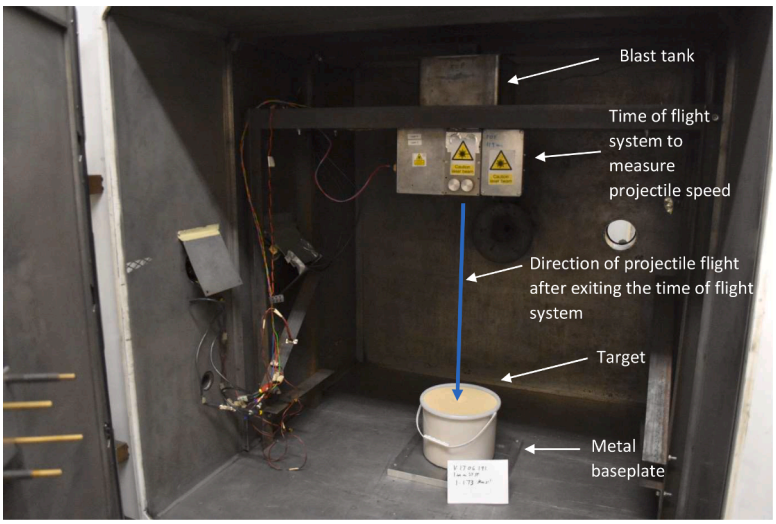


**Fig. 4.** Arrangement within target chamber, showing a sand target on the chamber floor. Various viewports and electrical feed-throughs are also visible in the walls of the chamber.

burst disc ruptured (approximately 80 bar). As can be seen in Fig. 5, by using the acetate-bursting disk, and changing the composition of the pressurizing gas, speeds in the range 0.3 to 1 km $s^{-1}$ were achieved. Most of the variation was obtained by moving from gases with a higher mean molecular mass such as nitrogen (low speed) to a lower mean molecular mass such as hydrogen (high speed). Some further variation in burst pressure was achieved with the acetate disc by waiting at a lower pressure for the disc to extrude and burst, or by pressurizing quickly to a higher pressure before extrusion occurred. Using different burst discs such as aluminium foil on an aluminium annular backing disc with a central aperture gives further speed selection options.

### 3.2. *Two stage gun performance in test firings*

The full two-stage vertical light-gas gun was tested with over 30 shots, again using a 1 mm diameter stainless steel sphere as the projectile. Speeds in the range 1 - 2 km $s^{-1}$ were obtained with the full pressure in the nitrogen gas reservoir (~300 bar) and by varying the pre-shot pressure of the hydrogen gas in the pump tube (Fig. 6). These shots used a 0.5 mm thick 2014 aluminium burst-disc, with a cross, or cross-plus-circle, punched into it to encourage the aluminium to petal outwards when it bursts. This petal forming does not work as consistently as it does with the horizontal gun which may be due to the lower mass of

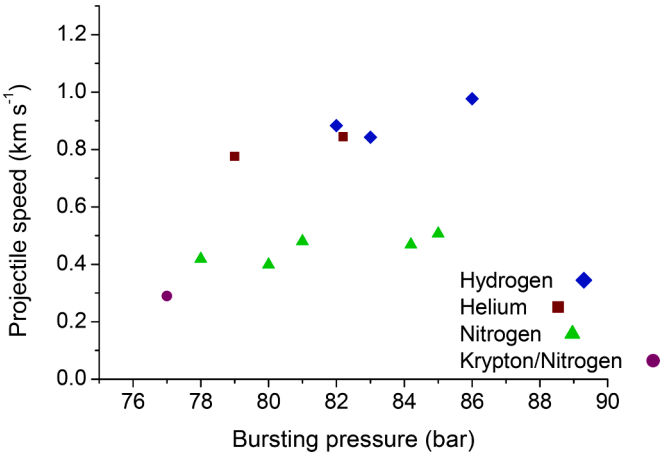


**Fig. 5.** Single stage vertical gun performance with various gases. The burst disk in all cases was made of acetate (0.25 mm thick).

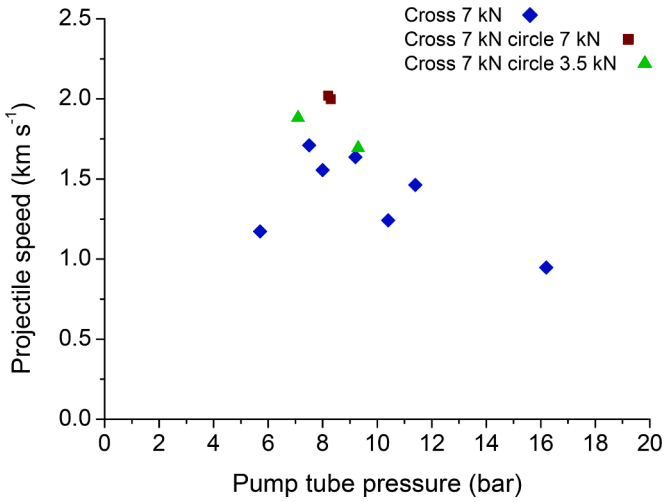


**Fig. 6.** Two stage vertical gun performance with hydrogen gas in the second stage and various burst-disc types. The bust-disks were aluminium, with cross-shaped and circular indentions to aid their rupture (indentation pressures as given in the legend). Two similar launch tubes were used (LT26 and LT34). The horizontal axis, gives the pre-shot pressure of the hydrogen gas in the pump tube, before it was further pressurised by the piston driven by the nitrogen gas when the release valve was opened.

hydrogen driving gas compared to that used for the horizontal gun. However, petal formation is desirable as the fragments are then more likely to travel off-axis and be intercepted in-flight by the stop-plate; they thus do not reach the target, giving a cleaner impact. Speeds below 1 km $s^{-1}$ were also achieved in the two-stage gun, by using acetate or copper bursting disks. There is some variation in the shot speed even if conditions are repeated (as with the single-stage gun) and is of order ± 4 % (similar to the original horizontal gun).

## 4. Analysis of data from test shots into sand

### 4.1. *Shot program*

While the gun was being commissioned, the opportunity was taken to generate impact data at normal incidence onto a granular target (sand). Sand was chosen to permit comparison with data in the literature (e.g. [24–26]). The sand used here had a typical grain diameter of 0.3 –

0.5 mm, a coefficient of friction (measured by slippage when tilted) of between 35° (onset of slippage) and 40° (full slippage of tilted sand). The density after settling in its container was 1670 ± 29 kg m$^{-3}$.

The sand container was placed on the target chamber floor beneath the vertical gun stop-plate. The target chamber was then evacuated to less than 1 mbar during each shot. The projectile speed was obtained in each shot. The projectiles were spheres made of stainless steel 420, 1.0 mm in diameter and density 7700 ± 100 kg m$^{-3}$. Six of the single stage, and thirty of the two-stage test shots yielded useful data (in a few of the earliest shots no sand target was used as the initial focus was on firing the gun successfully, and in one of the later shots a sabot fragment hit the target along with the projectile). As expected, the resulting impact craters were circular (see Fig. 7 for a typical depth profile across one crater). The crater depths and diameters were measured using caliper gauges. Crater depth was taken from the level of the original undisturbed surface to the floor of the crater. Two definitions of crater diameter were used, from rim to rim, and an inner diameter in the original surface plane (Fig. 7). In each crater, several measurements of each parameter were made and then averaged to give the uncertainty (which was larger than the instrument accuracy). Typical crater diameters are thus accurate to ± 1 mm. Crater depths are in principle accurate to ± 0.01 mm, but in practice are limited by the size of individual sand grains and are thus more likely of order ± 0.1 mm.

### 4.2. Shot results

All crater data are given in Table 1, and crater inner diameters and depths are plotted in Figs. 8 and 9 respectively. The data for inner crater diameter ($D_i$) were fit vs. impact speed (v) with both a linear function and a power law (the latter being more usual in cratering studies). We obtained:

$$D_i = (27.7 \pm 1.5) + (11.1 \pm 1.3)v \quad r = 0.8254 \tag{1}$$

$$D_p = (39.7 \pm 0.5)v^{(0.272 \pm 0.051)} \quad r = 0.8450 \tag{2}$$

where $D_i$ was in mm and v in km s$^{-1}$, with r giving the regression coefficient of each fit. No significant difference in goodness-of-fit was observed between the two types of fit over the range of crater size here. As expected the rim-to-rim diameters of the craters ($D_r$) were larger than

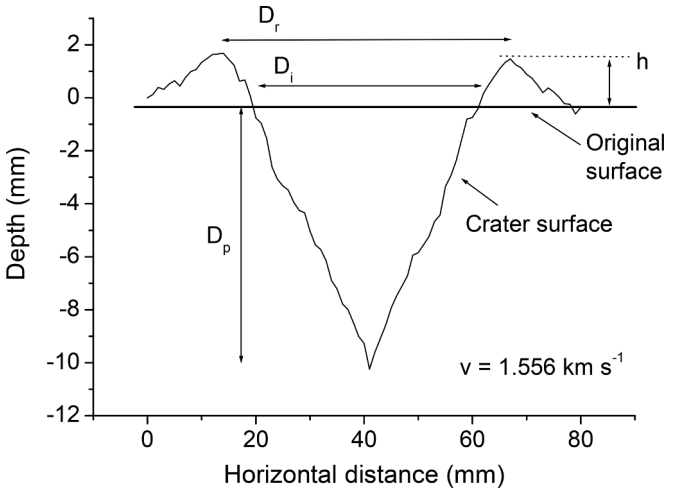


**Fig. 7.** Cross section across a typical crater. Crater depth is measured from the original surface level. Two measures of crater diameter are taken, rim to rim ($D_r$) and an inner diameter in the original surface plane ($D_i$). Crater depth ($D_p$) is measured from the original surface plane, as is the rim height (h). The example shown is a profile across the impact at 1.556 km s$^{-1}$, and was measured in 1 mm steps across the crater. Care was taken to ensure all profiles passed across the centres of the craters.

**Table 1**
Measurements of crater dimensions for impacts of a 1 mm diameter stainless steel sphere into sand. In some cases crater depth was not measured (marked "nm"). Speeds are accurate to ±1 %, crater diameters are typically accurate to ±1 mm and crater depth is accurate to ±0.1 mm.

| Speed (km $s^{-1}$) | Inner crater diameter (mm) | Crater depth (mm) | Single-Stage (SS) or Two-Stage (TS) |
|---|---|---|---|
| 0.289 | 25 | nm | SS |
| 0.327 | 27 | nm | TS |
| 0.399 | 33 | 8.04 | SS |
| 0.425 | 33 | 7.34 | TS |
| 0.469 | 32 | 8.61 | SS |
| 0.533 | 38 | 9.08 | TS |
| 0.625 | 36 | 9.96 | TS |
| 0.688 | 41 | 7.36 | TS |
| 0.776 | 38 | 8.58 | SS |
| 0.840 | 35 | 8.60 | TS |
| 0.844 | 32 | Nm | SS |
| 0.851 | 40 | 9.10 | TS |
| 0.883 | 39 | 9.06 | SS |
| 0.893 | 33 | 8.95 | TS |
| 0.944 | 32 | 9.22 | TS |
| 0.947 | 39 | 9.82 | TS |
| 1.067 | 43 | 9.93 | TS |
| 1.111 | 43 | 9.98 | TS |
| 1.115 | 45 | 7.93 | TS |
| 1.169 | 48 | 11.0 | TS |
| 1.173 | 43 | 7.73 | TS |
| 1.215 | 37 | 8.62 | TS |
| 1.228 | 41 | 9.91 | TS |
| 1.242 | 41 | 9.67 | TS |
| 1.269 | 41 | 8.77 | TS |
| 1.276 | 43 | 9.77 | TS |
| 1.312 | 43 | 7.91 | TS |
| 1.321 | 44 | 11.78 | TS |
| 1.358 | 46 | 11.76 | TS |
| 1.444 | 43 | 10.05 | TS |
| 1.463 | 42 | 10.70 | TS |
| 1.556 | 44 | 10.77 | TS |
| 1.640 | 40 | 11.99 | TS |
| 1.711 | 48 | 12.16 | TS |
| 2.00 | 49 | 13.21 | TS |
| 2.02 | 49 | 12.37 | TS |

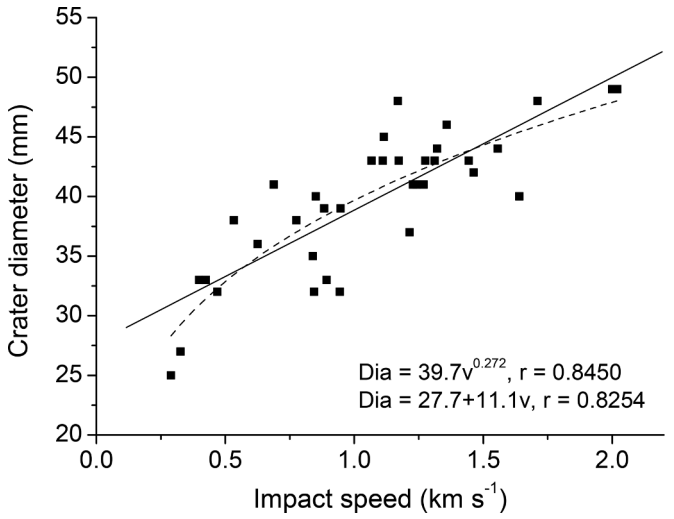


**Fig. 8.** Inner crater diameter vs. impact speed for 1 mm diameter stainless projectiles impacting sand. The solid line is a linear fit to the data, and the dashed line a power law fit.

the inner diameters, and a ratio of ($D_r$ / $D_i$) = (1.142 ± 0.045) was found, with no observed dependence on impact speed.

The data for crater depth ($D_p$) were also fit vs. impact speed (v) with both a linear function and a power law. We obtained:

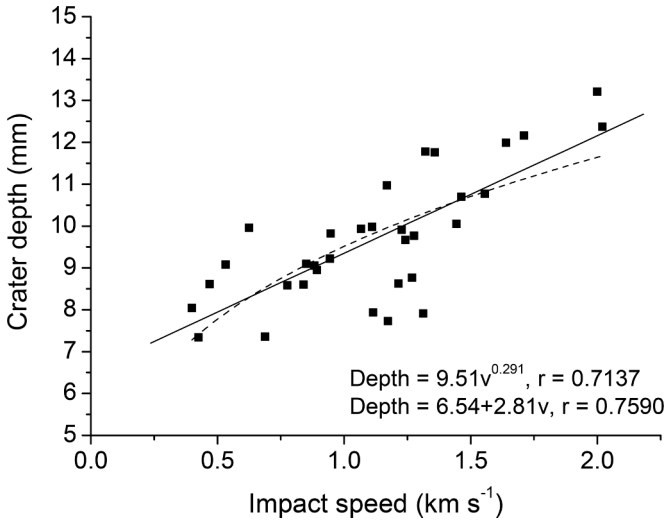


**Fig. 9.** Crater depth vs. impact speed for 1 mm stainless projectiles. The solid line is a linear fit to the data, and the dashed line a power law fit.

$$D_p = (6.54 \pm 0.52) + (2.81 \pm 0.43)v \qquad r = 0.7590 \tag{3}$$

$$D_p = (9.51 \pm 0.20)v^{(0.291 \pm 0.052)} \qquad r = 0.7137 \tag{4}$$

where $D_i$ was in mm and v in km $s^{-1}$, with r giving the regression coefficient of each fit. Again, no significant difference in goodness-of-fit was observed between the two types of fit.

The crater depth-to-diameter ratio, $D_p$ / $D_i$, was found to be 0.24 ±0.03 with a scatter that was too large to show any significant trend vs. impact speed. This is no surprise given the similar magnitude of the power law exponents in Eqs. (2) and (4) for crater depth and diameter vs. impact speed. This is compatible with Mizutani et al. [25] for impacts in loose quartz sand (density 1360 kg $m^{-3}$) at 35 – 830 m $s^{-1}$, who found a depth/diameter ratio of 0.25. It is, however, slightly larger, but still compatible with the result of [24], who for impacts into quartz sand at 0.7 and 1.3 km $s^{-1}$, found crater depth/diameter = 0.20 – 0.21.

The height of the crater rim (h) above the original sand surface level was also measured. We found that h was approximately (3.2 ± 1.2) % of the rim to rim diameter, albeit with significant scatter on the data, hence the large uncertainty. It has long been known that rim height for many small craters made in the laboratory, and even for small lunar craters (< 15 km), depends only weakly on crater rim-to-rim diameter, with Pike [27] reporting $h = 0.036D_r^{1.104}$. As noted by Melosh [28] this weak power is not significantly different from unity, suggesting that un-collapsed crater rims have a height some 3 - 4 % of the rim-to-rim diameter, compatible with that reported here. When normalized to the crater depth, i.e. $h/D_p$, no clear correlation was found with impact speed, with an average rim height of (10.7 ± 3.7) % of the crater depth.

### 4.3. Pi-scaled crater dimensions

Crater dimensions are often described as obeying pi-scaling, i.e. they can be scaled in dimensionless ratios of all key parameters controlling the impact process (see [28] for a discussion). In the case of essentially strength-less target materials, crater sizes are held to scale as in a gravity dominated regime. Thus the scaled crater diameter, $\pi_D$, scales with a term, $\pi_2$ according to a power law, and crater depth given by $\pi_H$ which similarly scales with $\pi_2$, such that:

$$\pi_D = C_d \pi_2^{-\beta}, \tag{5}$$

where

$$\pi_D = D_i(\rho_t/m)^{1/3}, \tag{6}$$

$$\pi_H = H(\rho_t/m)^{1/3}, \tag{7}$$

$$\pi_2 = 1.61gL/v^2, \tag{8}$$

with $\rho_t$ being target density, m the projectile mass, g the local gravity, L the projectile diameter and v the impact speed (all units are SI). The coefficient β is found by fits to data. Here we plot the data for $\pi_D$ vs. $\pi_2$ in Fig. 10a, and obtain a power-law fit to the data:

$$\pi_D = (2.57 \pm 0.73)\pi_2^{-(0.136 \pm 0.016)}, \tag{9}$$

with a regression coefficient of 0.8450. We similarly fit $\pi_H$ vs. $\pi_2$ in Fig. 10b, and obtain a power-law fit to the data:

$$\pi_H = (0.518 \pm 0.245)\pi_2^{-(0.146 \pm 0.026)}, \tag{10}$$

with a regression coefficient of 0.7137. The lower value of the regression coefficient reflecting greater scatter in the depth data compared to that for crater diameter.

Previous data exists for pi-scaling of impact craters in sand and is

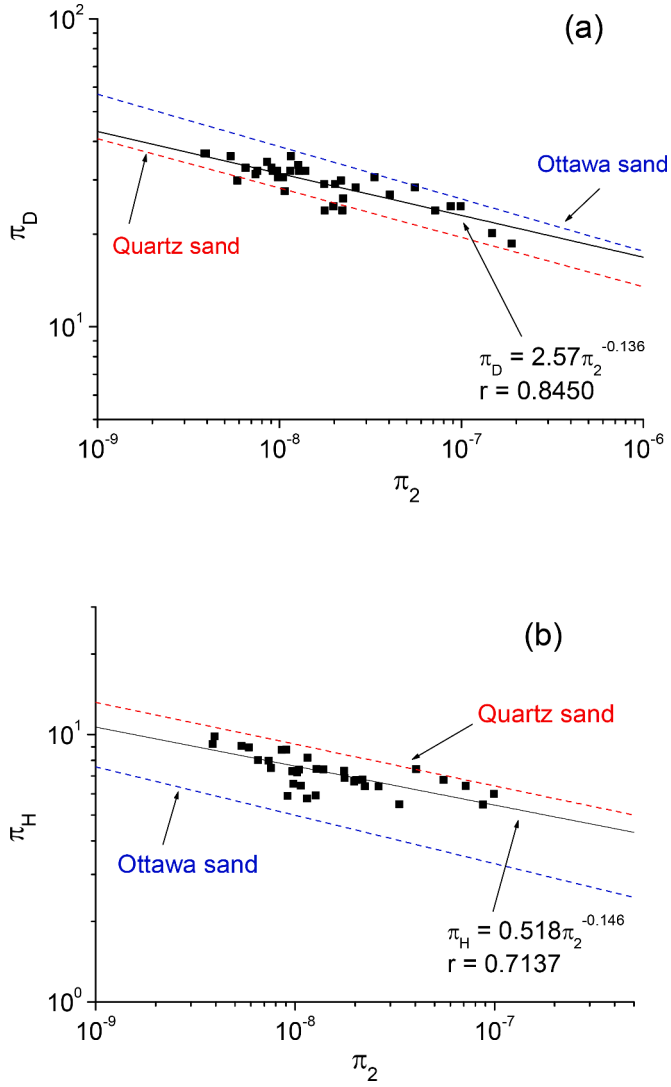


**Fig. 10.** The data for sand crater diameter and height vs. impact speed formed into pi-scaled variables $\pi_D$ and $\pi_H$ vs. $\pi_2$ ((a) and (b) respectively). The data are fit with a power law (solid line). The predictions from Schmidt [29] for quartz sand and Ottawa sand (as summarized by Melosh (1989) are also shown (red and blue dashed lines respectively). The data here are intermediate between the quartz and Ottawa sands.

summarized in Melosh [28] for quartz sand and Ottawa sand with, for diameter, $C_d = 1.4$ and 1.68 respectively, and $\beta = 0.16$ and 0.17 respectively. The results for the data here are intermediate between the predictions from the Ottawa and quartz sands (see Fig. 10). The original experiments for Ottawa sand are described in Schmidt [26] and cover an impact speed range of 2.1 to 7.25 km $s^{-1}$. The Ottawa sand had an angle of friction of 35°, whereas the quartz sand was 28° [26]. The former is compatible with the onset of slippage in the sand here of 35°, but the latter is slightly smaller. Schmidt [26] suggested that the angle of friction plays a significant role in the crater size. It should, however, also be noted that the data for both the Ottawa and quartz sand were taken in chambers at an ambient pressure of 1 atmosphere, unlike here where a vacuum chamber was used. To test the hypothesis that the friction angle plays a role in crater formation, Schmidt [26] plotted $\pi_H$ vs. $\pi_2$, and observed a significant difference with the friction angle (i.e. type of sand). Here we show $\pi_H$ vs. $\pi_2$ in Fig 10b, but again our data are intermediate between the results for quartz sand and Ottawa sand. It is thus not possible to confirm that the coefficient of friction is responsible for the variation in results between the data sets, and sand grain size or the ambient pressure cannot be ruled out as also playing a role.

Regarding sand grain size, [24], in their work on impacts at 0.7 and 1.3 km $s^{-1}$, used targets comprising three different sand grain sizes (0.5 mm, 0.5 – 1 mm, 1 – 2 mm), plus a mixed size target. They found that, at a fixed impact speed, crater depth did not change as the grain size in the targets was varied from <0.5 mm to 2 mm. Crater diameter did, however, change, being smaller at the small grain sizes in the shots at 1.3 km $s^{-1}$, but being a similar size independent of sand grain size at low speed (0.7 km $s^{-1}$). Overall, they were unable to determine if the differences they found were due to sand grain size, friction or slumping of the sand.

### 4.4. Projectile recovery post-shot

In 32 of the shots (0.399 – 2.020 km $s^{-1}$), we recovered the projectile from beneath the floor of the crater. In each case, the projectile was intact (Fig. 11). At the lowest speeds, there were some thin patches of sand adhered to the projectile surface in random locations. However, this changed as speed increased, and from 0.776 km $s^{-1}$ upwards, a distinct nose-cone of sand had adhered to one face of the projectile. We

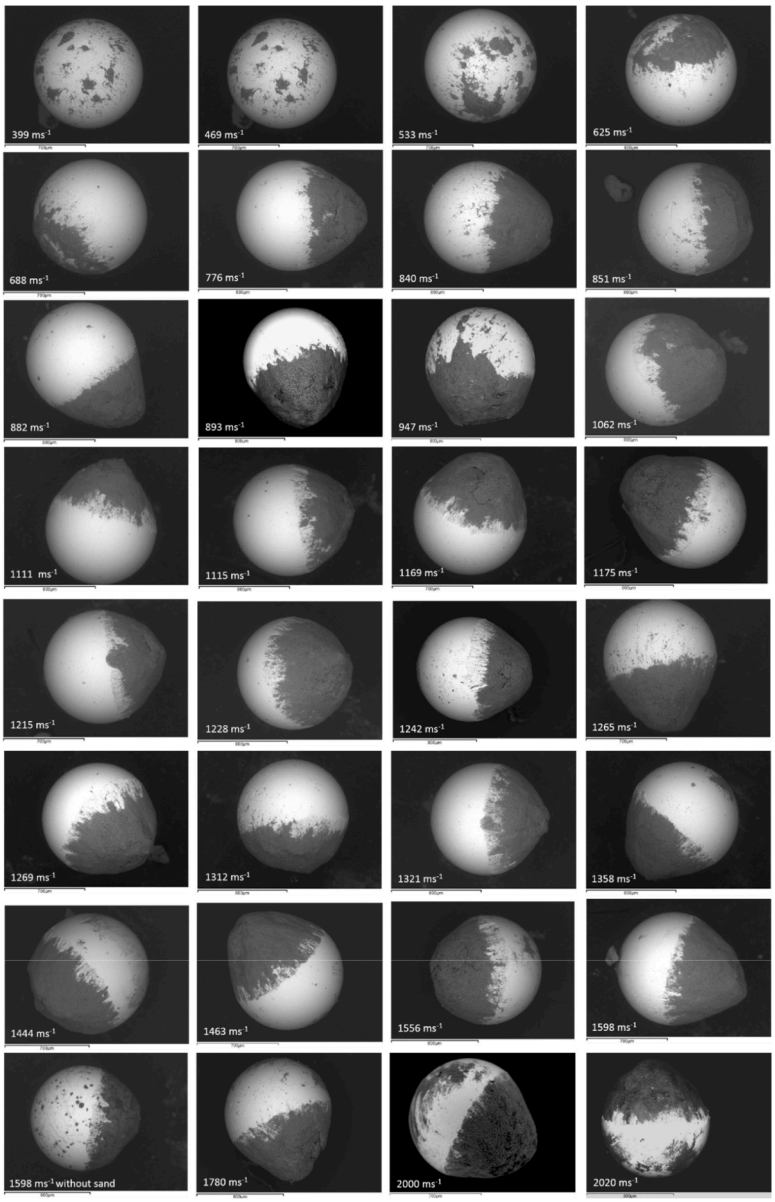


**Fig. 11.** Recovered projectiles from shots of 1 mm diameter stainless steel projectiles impacting sand. Sand can be seen coating parts of the projectile, forming a nose-cone in the higher speed impacts.

assume this nose-cone was on the leading face of the projectile during penetration into the sand. At the highest speed, 2.020 km $s^{-1}$, there is some indication that the projectile is slightly distorted in shape; the trailing (sand free) rear of the projectile is still spherical, but the nose-cone of sand on the leading face seems to overlay an eroded front hemisphere of the stainless steel projectile. Sculpting of the leading face of a stainless steel projectile during impact, was previously shown in Fig. 16 of [18], where impacts of a 0.5 mm diameter stainless steel sphere at 3.10 km $s^{-1}$ in aerogel of density 25 kg $m^{-3}$, resulted in heavy erosion of the leading face. Again the result was a nose-cone like shape of the projectile, albeit with a slightly raised rim around the equator of its equator.

To obtain an estimate of the peak shock pressure during impact we use the Planar Impact Approximation (PIA, e.g. see [28]). This uses data for the shock Hugoniot relying on the linear wave speed relationship of the form $U = C + Su$, where U is the shock speed and u is the particle speed. Values of C and U differ for the projectile and target materials, and are found from experiments. For stainless steel we use C = 4610 m $s^{-1}$ and S = 1.73 (taken from [30]), along with density 7700 kg $m^{-3}$. For sand there is a choice in the literature and accordingly we use two estimates of C and S (C = 243 m $s^{-1}$, S = 2.348, from [31] who used sand with a density of 1570 kg $m^{-3}$, and C = 402 m $s^{-1}$, $S = 1.60$, from [32], who used sand with a density of 1600 kg $m^{-3}$) to see how sensitive the results are. In both cases the sand density is roughly similar to that here. The predictions of peak shock pressure vs. impact speed are shown in Fig. 12, where we obtain that at 2 km $s^{-1}$, pressures are in the range 9.4 – 12.0 GPa. We can thus say that the projectile is intact at shock pressures to at least of order 10 GPa, but some erosion and/or ablation is starting to occur.

Interaction of the projectile with a target is a well-known phenomenon. In previous work, for example [33], we have shown that 1 mm diameter copper projectiles survive intact and retain their spherical shape, after impacts into porous ice at speeds up to 2 km $s^{-1}$. This was equivalent to a peak pressure during impact of 6.8 GPa. At higher speeds and shock pressures deformation occurred with the onset of fragmentation by 9 GPa, and increasing fragmentation from 10.4 GPa upwards, i.e., this occurs at lower pressures than here for stainless steel, reflecting the lower strength of the copper. For projectiles of basaltic glass (weaker still than both copper and stainless steel), the peak shock pressure necessary to disrupt the projectile is in the order of 1 – 1.5 GPa (see [34] for a discussion).

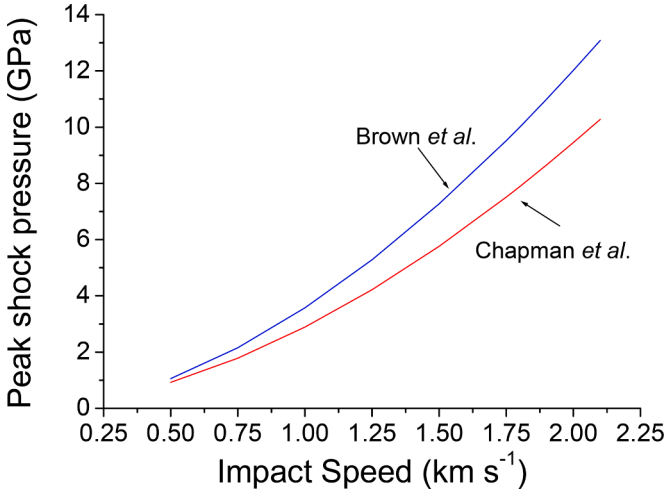


**Fig. 12.** Estimates of the peak impact shock pressure made using the Planar Impact Approximation. Two estimates are made, one using shock Hugoniot data for sand from [31], the other using data from [32].

## 5. Conclusions

The single and two stage guns have been shown to work as designed. The right-angled turn in the gun has not impeded performance, and speeds up to 2 km $s^{-1}$ have been achieved. The use of vaporized liquid nitrogen to produce high-pressure nitrogen gas to drive a two-stage gas gun has also been shown to be practical. The shot rate has been found to be one shot per day, but could be increased to two shots per day with more automation. The liquid nitrogen-filling loop could be made longer to reduce the number of filling operations required and provide more distance between the liquid nitrogen and the swaged connectors. The delivery tubing from the filling loop to the gas reservoir is currently 3 mm OD and 1.5 mm ID to give good gas temperature equalization with the room, and this may need to be increased in diameter if a longer filling loop is chosen.

Although only about 500 mL of liquid nitrogen was used to fill the gas reservoir per shot including wastage, a further 10 L was used to cool the filling loop. This is an acceptable expense per shot, but could be improved with a better fitting Dewar around the filling loop and more work on improving the way the cooling liquid nitrogen is used.

The use of these small-bore pipeline components has allowed the required speeds to be achieved and more optimization may allow higher speeds. A better gas reservoir design would include a larger internal diameter. This is a planned upgrade to this gun, with 16 mm OD 2.5 mm wall thickness tube, now that the highest required operating pressure for the reservoir of 340 bar has been established. Alternative safety burst discs have also been obtained rated at 374 bar (note that the safety burst-discs are only available in discrete values, and the error in its operating pressure must be above the required 340 bar and below the 16 mm tube pressure rating of 400 bar). An additional improvement already planned is to the sabots. At the moment the existing set-up permits firing of single, large projectiles. By crimping the end of the sabot, it is hoped to be able to retain multiple small ($< 100$ μm) projectiles in the sabot and fire a cloud of such projectiles in a shot, as can be done with the horizontal gun (e.g., see [35]).

To demonstrate the performance of the gun, cratering in sand targets is reported. As well as the classic early experiments regarding cratering in sand reported in the 1970s and 80 s, sand cratering experiments are still reported today (e.g. [24]). The results obtained here for cratering in sand over a wide speed range are shown to be compatible with previous work.

Now that the gun is operational, several new programs can be undertaken. The new vertical gun already overlaps the lower speed regime of the present gun and any work at those speeds in the horizontal gun can now also be undertaken with water or low-cohesion targets. For example, in planetary science there are various niche areas of impacts that occur at speeds up to 2 km $s^{-1}$. These include implantation of Martian ejecta into Phobos and Deimos (where impact speeds are estimated to cover 1 – 4.5 km $s^{-1}$, see Chappaz et al., 2013, so the vertical gun can already cover the lower end of that range), or the capture of materials in the plumes of Io and Enceladus during orbits of those bodies (e.g. see [36]). There have also been specific examples of impacts in the gun's speed range arising from human activities in space. For example, the ESA Smart-1 spacecraft impacted the Moon at its end-of-life in an impact at 2.1 km $s^{-1}$ [19,20]. Fortunately, the impact was at a shallow angle, so the impact into a loose regolith could be simulated in the horizontal gun. This can now be reproduced over a much wider range of impact angles in future. In addition, impact testing of material response to impacts at speeds up to 2 km $s^{-1}$ can now be undertaken, with the crater site retained intact after impact without the added complication of material falling away from the crater under gravity after the impact process has completed. In particular, impact cratering events in water can now be studied without the water flowing away after impact, as was the case with earlier studies in the horizontal Kent gun [21,22]. Combined with the planned upgrade to increase the impact speed, a wide range of activities are thus planned.

## CRediT authorship contribution statement

**M.C. Price:** Conceptualization, Funding acquisition, Investigation, Methodology, Writing – review & editing. **M.J. Cole:** Conceptualization, Formal analysis, Investigation, Methodology, Writing – review & editing. **K.H. Harriss:** Formal analysis, Investigation, Methodology, Writing – review & editing. **L.S. Alesbrook:** Investigation, Writing – review & editing. **M.J. Burchell:** Funding acquisition, Investigation, Methodology, Formal analysis, Project administration, Writing – original draft, Writing – review & editing. **P.J. Wozniakiewicz:** Investigation, Project administration, Writing – review & editing.

## Declaration of Competing Interest

The authors declare that they have no known competing financial interests or personal relationships that could have appeared to influence the work reported in this paper.

## Data availability

Data will be made available on request.

## Acknowledgments

The authors would like to thank the Royal Society for an instrument development grant (RG140480) and the STFC for funding via a consolidated grant ST/S000348/1. We would also like to thank the University of Kent for a development grant. D. Doherty is thanked for assistance early in this project.

## References

[1] Burchell MJ, et al. Hypervelocity impact studies using the 2 MV Van de Graaff accelerator and two-stage light gas gun of the University of Kent at Canterbury. Meas Sci Technol 1999;10(1):41–50.
[2] Hibbert R, et al. The hypervelocity impact facility at the University of Kent: recent upgrades and specialized capabilities. Procedia Eng 2017;204:208–14.
[3] Crozier WD, Hume W. High velocity, light gas gun. J Appl Phys 1957;28:892–8.
[4] Rogers JA, et al. The Texas A&M university hypervelocity impact laboratory: a modern aeroballistic range facility. Rev Sci Instrm 2022;93:085106. https://doi.org/10.1063/5.0088994.
[5] Karcz JS, Bowling D, Cornelison C, Parrish A, Perez A, Raiche G, et al. The Ames vertical gun range. In: 47th Lunar and Planetary Science Conference (2016). Houston, TX, USA; 2016. abstract 2599.
[6] McDonnell JAM. The Open University planetary impact facility: a compact two-stage light gas gun for all impact angles. Int J Impact Eng 2006;33:410–8.
[7] See TH, Cardenas F, Montes R. The Johnson space center experimental impact lab: contributions toward understanding the evolution of the solar system. 43rd Lunar and Planetary Science Conference (2012). Houston, TX, USA; 2012. abstract #2488.
[8] Kawai N, Zama S, Takemoto W, Moriguchi K, Arai K, Hasegawa S, Sato E. Stress wave and damage propagation in transparent materials subjected to hypervelocity impact. Procedia Eng 2015;103:287–93.
[9] Cornwell LT, Wozniakiewicz PJ, Burchell MJ, Alesbrook LA, Corsaro RD, Giovane F, Liou J-C. A study on the capabilities and accuracy of Kapton based TOF space dust and debris detector. Accepted in Adv Space Res 2023. https://doi.org/10.1016/j.asr.2022.07.022.
[10] Warren JJ, Cole M, Offenberger S, Kota KR, Lacy TE, Toghiani H, Burchell M, Kundu S, Pittman Jr CU. Hypervelocity impacts on honeycomb core sandwich panels filled with shear thickening fluid. Int J Impact Eng 2021;150:103803. https://doi.org/10.1016/j.ijimpeng.2020.103803.
[11] Fisher CR, Price MC, Burchell MJ. Salt grains in hypervelocity impacts in the laboratory. Meteor Planet Sci 2021;56(9):1652–68. https://doi.org/10.1111/maps.13729.
[12] Burchell MJ, Harriss KH. Catastrophic disruption by hypervelocity impact of multi-layered spherical ice targets. Int J Impact Engng 2022;168:104294. https://doi.org/10.1016/j.ijimpeng.2022.104294.
[13] Price MC, Kearsley AT, Burchell MJ. Validation of the Preston-Tonks-Wallace strength model at strain rates of $10^{13}$ $s^{-1}$ for Al-1100, Tantalum and Copper using hypervelocity impact crater morphologies. Int J Impact Eng 2013;52:1–10. A.
[14] Doolan JA, Alesbrook LS, Baker K, et al. Next-generation protein-based materials capture and preserve projectiles from supersonic impacts. Nat Nanotechnol 2023;18:1060–6. https://doi.org/10.1038/s41565-023-01431-1.
[15] Martins Z, Price MC, Goldman N, Sephton MA, Burchell MJ. Shock synthesis of amino acids from impacting cometary and icy planet surface analogues. Nat Geosci 2013;6:1045–9.
[16] Singh SV, Dilip H, Meka JK, Thiruvenkatam V, Vishakantaiah J, Muruganathan M, Vijayan S, Rajasekhar BN, Bhardwaj A, Mason N, Burchell MJ, Sivaraman B. New signatures of bio-molecular complexity in the hypervelocity impact ejecta of icy moon analogues. Life 2022;12(4):508. https://doi.org/10.3390/life12040508. 12 pp.
[17] Price MC, Solscheid C, Burchell MJ, Josse L, Adamek N, Cole MJ. Survival of yeast spores in hypervelocity impact events upto velocities of 7.4 km $s^{-1}$. Icarus 2013;222:263–72.
[18] Burchell MJ, Fairey SAJ, Foster NJ, Cole MJ. Hypervelocity capture of particles in aerogel: dependence on aerogel properties. Planet Space Sci 2009;57:58–70.
[19] Burchell MJ, Robin-Williams R. Foing B.H. and the SMART-1 impact team. The SMART-1 lunar impact. Icarus 2010;207:28–38.
[20] Burchell MJ, Cole MJ, Ramkissoon NK, Wozniakiewicz PJ, Price MC, Foing B. Smart-1 end of life shallow regolith impact simulations. Meteorit Planetary Sci 2015;50:1436–48. https://doi.org/10.1111/maps.12479.
[21] Milner DJ, Baldwin EC, Burchell MJ. Laboratory investigations of marine impact events: factors influencing crater formation and projectile survivability. Meteor Planet Sci 2008;43:2015–26.
[22] Baldwin EC, Milner DJ, Burchell MJ, Crawford IA. Laboratory impacts into dry and wet sandstone with and without an overlying water layer: implications for scaling laws and projectile survivability. Meteorit Planetary Sci 2007;42:1905–14.
[23] Gores PAS, Spray JG. Hypervelocity impact of anorthosite: excavation, spallation and crater reconstruction. Int J Impact Eng 2022;160:104078.
[24] Mazur R, Beczek M, Janiszewski J, Koperski W, Polakowski C, Fikus B, et al. Experimental investigations of crater formation as a result of high-velocity impacts on sand bed. PLoS ONE 2022;17(3):e0265546. https://doi.org/10.1371/journal.pone.0265546.
[25] Mizutani H, Kawakami S, Takagi Y, Kato M, Kumazawa M. Cratering experiments in sands and a trial for general scaling law. J Geophys Res 1983;88:A835–54. https://doi.org/10.1029/JB088iS02p0A835.
[26] Schmidt RM. Meteor crater: energy of formation – implications of centrifuge scaling. Proc Lunar Planet Sci Conf 11th 1980:2099–128. pp.
[27] Pike R.J. Size-dependence in the shape of fresh impact craters on the moon. In: Impact and explosive cratering (editors Roddy D.J., Peppin R.O., and Merrill R.B.), Pergamon Press, New York, 1977.
[28] Melosh HJ. Impact cratering: a geological process. Pub Oxford; 1989.
[29] Schmidt RA, Housen KR. Some recent advances in the scaling of impact and explosion cratering. Int J Impact Engng 1987;5:543–60.
[30] Parnell J, Bowden S, Lindgren P, Burchell MJ, Milner D, Baldwin EC, Crawford IA. The preservation of fossil biomarkers during hypervelocity impact experiments using organic rich siltstones as both projectiles and targets. Meteor Planet Sci 2010;45:1340–58.
[31] Brown JL, et al. Shock response of dry sand. Sandia Rep 2007:2007–3524. https://www.osti.gov/servlets/purl/913227.
[32] Chapman DJ, Tsembelis K, Proud WG. The behaviour of dry sand under shock loading. In: Furnish MD, Elert M, Russell TP, White CT, editors. CP845 Shock Compression of Condensed Matter–2005: AIP Conference Proceedings; 2006. p. 1445–8.
[33] McDermott KH, Price MC, Cole M, Burchell MJ. Survivability of copper projectiles during hypervelocity impacts in porous ice: a laboratory investigation of the survivability of projectiles impacting comets or similar bodies. Icarus 2016;268:102–17. https://doi.org/10.1016/j.icarus.2015.12.037.
[34] Wickham-Eade JE, Burchell MJ, Price MC, Harriss KH. Hypervelocity impact fragmentation of Basalt and Shale projectiles. Icarus 2018;311:52–68. https://doi.org/10.1016/j.icarus.2018.03.017.
[35] Chan DH, Millet A, Fisher CR, Price MC, Burchell MJ, Armes SP. Synthesis and characterization of polypyrrole-coated anthracene microparticles: a new synthetic mimic for polyaromatic hydrocarbon-based cosmic dust. ACS Appl Mater Interfaces 2021;13(2):3175–85. https://doi.org/10.1021/acsami.0c19758.
[36] Traspas A, Burchell MJ. Tardigrade survival limits in high speed impacts – implications for panspermia and collection of samples from plumes emitted by ice worlds. Astrobiology 2021;21(7):845–52. https://doi.org/10.1089/ast.2020.2405.